Cosmic voids and void lensing in the Dark Energy Survey Science Verification data

C. Sánchez,[1]* J. Clampitt,[2] A. Kovacs,[1] B. Jain,[2] J. García-Bellido,[3] S. Nadathur,[4]
D. Gruen,[5,6]† N. Hamaus,[7] D. Huterer,[8] P. Vielzeuf,[1] A. Amara,[9] C. Bonnett,[1]
J. DeRose,[5,10] W. G. Hartley,[9,11] M. Jarvis,[2] O. Lahav,[11] R. Miquel,[1,12] E. Rozo,[13]
E. S. Rykoff,[5,6] E. Sheldon,[14] R. H. Wechsler,[5,6,10] J. Zuntz,[15] T. M. C. Abbott,[16]
F. B. Abdalla,[11,17] J. Annis,[18] A. Benoit-Lévy,[11,19,20] G. M. Bernstein,[2]
R. A. Bernstein,[21] E. Bertin,[19,20] D. Brooks,[11] E. Buckley-Geer,[18]
A. Carnero Rosell,[22,23] M. Carrasco Kind,[24,25] J. Carretero,[1,26] M. Crocce,[26]
C. E. Cunha,[5] C. B. D'Andrea,[4,27] L. N. da Costa,[22,23] S. Desai,[28,29] H. T. Diehl,[18]
J. P. Dietrich,[28,29] P. Doel,[11] A. E. Evrard,[9,30] A. Fausti Neto,[22] B. Flaugher,[18]
P. Fosalba,[26] J. Frieman,[18,31] E. Gaztanaga,[26] R. A. Gruendl,[24,25] G. Gutierrez,[18]
K. Honscheid,[32,33] D. J. James,[16] E. Krause,[5] K. Kuehn,[34] M. Lima,[22,35]
M. A. G. Maia,[22,23] J. L. Marshall,[36] P. Melchior,[37] A. A. Plazas,[38] K. Reil,[6]
A. K. Romer,[39] E. Sanchez,[3] M. Schubnell,[8] I. Sevilla-Noarbe,[3] R. C. Smith,[16]
M. Soares-Santos,[18] F. Sobreira,[22,40] E. Suchyta,[41] G. Tarle,[8] D. Thomas,[4]
A. R. Walker,[16] J. Weller[7,28,42] and The DES Collaboration

Affiliations are listed at the end of the paper

ABSTRACT

Cosmic voids are usually identified in spectroscopic galaxy surveys, where 3D information about the large-scale structure of the Universe is available. Although an increasing amount of photometric data is being produced, its potential for void studies is limited since photometric redshifts induce line-of-sight position errors of ≥ 50 Mpc h^{-1} which can render many voids undetectable. We present a new void finder designed for photometric surveys, validate it using simulations, and apply it to the high-quality photo-z redMaGiC galaxy sample of the DES Science Verification data. The algorithm works by projecting galaxies into 2D slices and finding voids in the smoothed 2D galaxy density field of the slice. Fixing the line-of-sight size of the slices to be at least twice the photo-z scatter, the number of voids found in simulated spectroscopic and photometric galaxy catalogues is within 20 per cent for all transverse void sizes, and indistinguishable for the largest voids ($R_v \geq 70$ Mpc h^{-1}). The positions, radii, and projected galaxy profiles of photometric voids also accurately match the spectroscopic void sample. Applying the algorithm to the DES-SV data in the redshift range $0.2 < z < 0.8$, we identify 87 voids with comoving radii spanning the range 18–120 Mpc h^{-1}, and carry out a stacked weak lensing measurement. With a significance of 4.4σ, the lensing measurement confirms that the voids are truly underdense in the matter field and hence not a product of

Poisson noise, tracer density effects or systematics in the data. It also demonstrates, for the first time in real data, the viability of void lensing studies in photometric surveys.

Key words: gravitational lensing: weak – cosmology: observations – large-scale structure of Universe.

1 INTRODUCTION

Cosmic voids are low-density regions in space surrounded by a network of dark matter haloes and the galaxies which populate them. Given their intrinsic low-density environment, voids are only weakly affected by complicated non-linear gravitational effects which have a strong impact in crowded environments such as galaxy clusters. This simplicity makes it possible to constrain cosmological parameters with voids (Betancort-Rijo et al. 2009; Lavaux & Wandelt 2010; Sutter et al. 2014b; Kitaura et al. 2016; Hamaus et al. 2016; Mao et al. 2016; Sahlén, Zubeldía & Silk 2016). Furthermore, the unique low-density environments of voids make possible probes of the nature of dark energy, alternate theories of gravity (Lee & Park 2009; Bos et al. 2012; Spolyar, Sahlén & Silk 2013; Barreira et al. 2015; Cai, Padilla & Li 2015), and primordial non-Gaussianity (Song & Lee 2009).

A number of different void-finding algorithms exist in the literature: Voronoi tessellation and watershed methods (Platen, Van De Weygaert & Jones 2007; Neyrinck 2008; Lavaux & Wandelt 2012; Sutter et al. 2012; Nadathur et al. 2015), growth of spherical underdensities (Hoyle & Vogeley 2002; Colberg et al. 2005; Padilla, Ceccarelli & Lambas 2005; Ceccarelli et al. 2006; Li 2011), hybrid methods (Jennings, Li & Hu 2013), 2D projections (Clampitt & Jain 2015), dynamical criteria (Elyiv et al. 2015), and Delaunay triangulation (Zhao et al. 2016), among other methods (Colberg et al. 2008). Most void finders currently applied to data use galaxies with spectroscopic redshifts to define voids. However, when using far less precise photometric redshifts (photo-zs), the void-finding process needs to be revisited to overcome the smearing in the line-of-sight (LOS) position of tracer galaxies.

Spectroscopic surveys like 2dF (Colless et al. 2001), VVDS (Le Fèvre et al. 2005), WiggleZ (Drinkwater et al. 2010) or BOSS (Dawson et al. 2013) provide 3D information of the galaxy distribution, but they are expensive in terms of time, and may suffer from selection effects, incompleteness and limited depth. In contrast, photometric surveys such as SDSS (York et al. 2000), PanSTARRS (Kaiser, Tonry & Luppino 2000), KiDS (de Jong et al. 2013) or LSST (Tyson et al. 2003) are more efficient and nearly unaffected by selection bias, more complete and deeper, but do not provide complete 3D information of the galaxy distribution due to their limited resolution in the galaxy LOS positions, obtained by measuring the photo-z of each galaxy from the fluxes measured through a set of broad-band filters.

A few void catalogues exist which use photometric redshift tracers (Granett, Neyrinck & Szapudi 2008). Many voids about the size of the photo-z error or smaller will not be found at all; in other cases, spurious, or *Poisson*, voids will appear in the sample due to photo-z scatter. For the larger voids in the sample, those with sizes much larger than the photo-z error, the photo-z scatter should not affect the void sample substantially. However, these huge voids are very few due to the rapidly falling size distribution of cosmic voids in the universe. In any case, it should also be possible to find voids smaller than the photo-z scatter, since the latter acts to smooth out the density field, but retains the topology of the large-scale structure to some extent. Therefore, by designing a void-finding algorithm specifically for photometric redshift

surveys, the purity and completeness of the resulting void sample can be improved.

Qualitatively, our void-finding method can be understood with an analogy to galaxy clustering measurements. In that case, the ideal scenario is to measure the 3D correlation function of galaxies when spectroscopic redshifts are available. However, for photometric survey data sets, one usually avoids computing the 3D correlation function of galaxies because of the photo-z dispersion affecting the LOS component. The standard approach is therefore to split galaxies into tomographic photometric redshift bins, and compute the 2D angular correlation function in the projection of each of these LOS bins. The photometric redshift errors make the actual size of the redshift bins to be effectively comparable or larger than the photo-z scatter (see for instance Crocce et al. 2011). Then, in order to minimize the noise in the measurement, the optimal approach is to set the width of the redshift bins to be comparable or larger than the photo-z scatter. Finally, one measures the angular clustering in each of these redshift bins, and hence the evolution of clustering with redshift. In this work, we present a void finder which follows the same approach: finding voids in the angular projection of the galaxy distribution in redshift slices which are broader than the photo-z dispersion, and then combining the slices to get the most of the LOS information in the data.

Before applying the algorithm to the DES Science Verification (DES-SV) data set, we use simulations with mock spectroscopic and realistic photometric redshifts to validate the method, running the void finder in both cases and studying the differences among the void catalogues coming from the corresponding projected slices. Once the DES-SV void catalogue is defined, we measure the weak gravitational lensing signal around voids and confirm the voids are also empty in the dark matter.

The plan of the paper is as follows. In Section 2, we describe the Dark Energy Survey Science Verification data used in this paper, together with the simulations used to test the validity of the finder. Section 3 presents the 2D angular void finder algorithm and some simulation tests comparing the algorithm output when using spectroscopic and photometric redshifts for the tracer galaxies. Then, in Section 4, we apply the algorithm to DES-SV data and discuss the choice of redshift slices and the way we deal with survey edge effects. Finally, in Section 5, we use the final DES-SV void catalogue to measure the weak gravitational lensing around voids and we discuss our results and conclusions in Section 6.

2 DATA AND SIMULATIONS

The Dark Energy Survey (DES; Flaugher 2005; Flaugher et al. 2015; Dark Energy Survey Collaboration et al. 2016) is a photometric redshift survey which will cover about one eighth of the sky (5000 deg²) to a depth of $i_{AB} < 24$, imaging about 300 million galaxies in five broad-band filters (*grizY*) up to redshift $z = 1.4$. The DES camera (DECam; Flaugher et al. 2015) includes sixty-two 2048×4096 science CCDs, four 2048×2048 guider CCDs and eight 2048×2048 focus and alignment chips, for a total of 570 megapixels. In this paper, we use 139 deg² of data from the Science Verification (SV) period of observations (Diehl et al. 2014), which provided science-quality data at close to the nominal depth of the survey.

In a photometric redshift survey, such as DES, the photo-zs of tracer galaxies will impact the identification of voids with sizes comparable to the photo-z scatter σ_z, in a way which renders some voids smeared and undetected. For DES main galaxies, this is a problem since $\sigma_z \simeq 0.1$ (Sánchez et al. 2014), corresponding to $\sim$220 Mpc h^{-1} at $z = 0.6$, and typical voids have a comoving size of about 10–100 Mpc h^{-1}. However, we do not need to use all DES galaxies as void tracers. Instead, we can restrict ourselves to the luminous red galaxies (LRGs) in the sample, which are still good tracers of the large-scale structure and have much better photo-z resolution.

2.1 Void tracer galaxies: the redMaGiC catalogue

The DES-SV redMaGiC catalogue (Rozo et al. 2016) presents excellent photo-z performance: redMaGiC photometric redshifts are nearly unbiased, with median bias $(z_{spec} - z_{phot}) \approx 0.5$ per cent, a scatter $\sigma_z/(1 + z) \approx 1.70$ per cent, and a ≈ 1.4 per cent 5σ redshift outlier rate. That scatter corresponds to a redshift resolution of $\sim$50 Mpc h^{-1} at $z = 0.6$, a substantial improvement over DES main galaxies. Next, we summarize the redMaGiC selection algorithm, but we refer the reader to Rozo et al. (2016) for further details.

The red-sequence Matched-filter Galaxy Catalog (redMaGiC; Rozo et al. 2016) is a catalogue of photometrically selected LRGs. We use the terms redMaGiC galaxies and LRG interchangeably. Specifically, redMaGiC uses the redMaPPer-calibrated model for the colour of red-sequence galaxies as a function of magnitude and redshift (Rykoff et al. 2014). This model is used to find the best-fitting photometric redshifts for all galaxies under the assumption that they are red-sequence members, and the χ^2 goodness-of-fit of the model is then computed. For each redshift slice, all galaxies fainter than some minimum luminosity threshold L_{min} are rejected. In addition, redMaGiC applies a cut $\chi^2 \leq \chi^2_{max}$, where the cut χ^2_{max} as a function of redshift is chosen to ensure that the resulting galaxy sample has a constant space density $\bar{n}$. In this work, we set $\bar{n} = 10^{-3} h^3$ Mpc^{-3} with ΛCDM cosmological parameters $\Omega_\Lambda = 0.7$, $h_0 = 100$, and redMaGiC galaxies are selected in the redshift range $0.2 < z < 0.8$. We expect the redMaGiC galaxy selection to be only marginally sensitive to the cosmological parameters assumed (see Rozo et al. 2016 for details). The luminosity cut is $L \geq L_*(z)/2$, where the value of $L_*(z)$ at $z = 0.1$ is set to match the redMaPPer definition for SDSS (Rykoff et al. 2014), and the redshift evolution for $L_*(z)$ is that predicted using a simple passive evolution starburst model at $z = 3$ (Bruzual & Charlot 2003).

We use the redMaGiC sample because of the exquisite photometric redshift performance of the redMaGiC galaxy catalogue. Also, because void properties depend on the tracer sample used, the constant comoving density of redMaGiC tracers helps in assuring the resulting voids have similar properties. For example, the dark matter profile (Sutter et al. 2014a) and void bias (Chan, Hamaus & Desjacques 2014; Clampitt, Jain & Sánchez 2016a; Pollina et al. 2016) have been shown to depend on the tracer density or tracer bias used to define voids.

Aside from the data catalogue presented above, in this work, we also use ΛCDM simulations which mimic the properties of the DES-SV redMaGiC data set. The mock galaxy catalogue is the Buzzard-v1.0 from the Blind Cosmology Challenge (BCC) simulation suite, produced for DES (Wechsler et al., in preparation). These catalogues have previously been used for several DES studies (see e.g. Becker et al. 2016; Chang et al. 2015; Leistedt et al. 2016; Clampitt et al. 2016b; Kwan et al. 2017). The underlying N-body simulation is based on three cosmological boxes, a 1050 Mpc h^{-1} box with

1400^3 particles, a 2600 Mpc h^{-1} box with 2048^3 particles and a 4000 Mpc h^{-1} box with 2048^3 particles, which are combined along the LOS producing a light cone reaching DES full depth. These boxes were run with LGadget-2 (Springel 2005) and used 2LPTic initial conditions (Crocce, Pueblas & Scoccimarro 2006) with linear power spectra generated with CAMB (Lewis & Bridle 2002). ROCKSTAR (Behroozi, Wechsler & Wu 2013) was utilized to find haloes in the N-body volumes. The ADDGALS algorithm (Wechsler 2004; Busha et al. 2013; Wechsler et al., in preparation) is used to populate the dark matter simulations with galaxies as a function of luminosity and colour. ADDGALS uses the relationship between local dark matter density and galaxy luminosity, to populate galaxies directly on to particles in the low-resolution simulations. This relationship is tuned to reproduce the galaxy–halo connection in a higher resolution tuning simulation, in which galaxies are assigned using subhalo abundance matching (e.g. Conroy, Wechsler & Kravtsov 2006; Reddick et al. 2013), in this case, matching galaxy luminosity to peak circular velocity. Finally, each galaxy is assigned a colour by using the colour–density relationship measured in the SDSS (Aihara et al. 2011) and evolved to match higher redshift observations. The redMaGiC algorithm has been run on the simulation in a similar way as it is run on the DES data. This produces a simulated sample with the same galaxy selection and photometric redshift performance as the DES-SV redMaGiC catalogue but gives us access to the true redshifts of the galaxies in the sample, a fact which we will use to test the void finder presented in this work.

2.2 Lensing source catalogue

The catalogue of galaxy shapes used in the lensing measurement of this work is the `ngmix`[1] catalogue presented in Jarvis et al. (2016). `ngmix` is a shear pipeline which produces model fitting shape measurements, and which was applied to a large subset of DES-SV galaxies, meeting the requirements of an extensive set of null and systematics tests in Jarvis et al. (2016). The photometric redshifts of the galaxies in the `ngmix` shear catalogue were studied in detail in Bonnett et al. (2016), using four different photo-z codes. In this work, we use the SkyNet photo-z method, which demonstrated excellent performance in that comparison.

3 PHOTO-Z VOID FINDER ALGORITHM

In this section, we present a new void finder designed specifically to work on photometric surveys. We explain the algorithm and test its performance on simulations, providing validation for the results shown later in the paper.

3.1 Void finder algorithm

The void finder works by projecting galaxies in redshift slices and finding underdensities in the 2D angular distribution of galaxies in the given slices. If the LOS width of the projected slice is sufficiently large, at least about twice the photo-z resolution, then most galaxies will still be assigned to the correct slice. Since the finder works by projecting all galaxies within a given slice on to a 2D surface, the LOS position within the slice does not affect the results.

The void finder of Clampitt & Jain (2015) also begins by treating each slice in isolation, but has the disadvantage that voids are required to be completely empty of galaxies near the centre. Thus,

---

[1] https://github.com/esheldon/ngmix
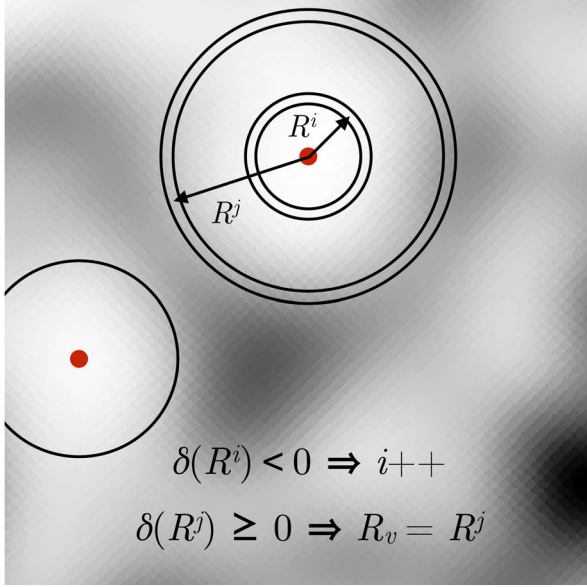
Figure 1. Graphical description of the void-finding algorithm presented in this paper. The background grey-scaled field is the smoothed galaxy field ($\sigma = 10$ Mpc h^{-1}) in a redshift slice used by the void-finder. The two filled (red) dots show two void centres. For the upper void, we show a circular shell or radius R^i. Since the density contrast $\delta(R^i) < 0$, the algorithm checks larger shells, up to radius R^j such that $\delta(R^j) \geq 0$. The void radius is then defined as $R_v = R^j$.

photo-z scatter, which moves a single galaxy between slices, can inappropriately break up a single large void into several smaller voids, or even result in no void being detected at all. To overcome this problem, we smooth the 2D projected galaxy density field in each slice and then voids are found from minima of the smoothed density field. This means a few galaxies moving between different slices will not greatly affect the resulting set of voids, as is demonstrated in Section 3.2.

In detail, the void-finding algorithm involves the following steps:

(i) We select the galaxies from a redshift slice of thickness $2s_v$ (we define s_v to be half the slice thickness) and we project them into a HEALpix map (Gorski et al. 2005), with a resolution of $N_{\text{side}} = 512$ representing an angular resolution of $0^\circ\!.1$ and a physical resolution of 1.5 Mpc h^{-1} at $z = 0.3$ (3 Mpc h^{-1} at $z = 0.6$).

(ii) We compute the mean density in the map corresponding to the given redshift slice, $\bar{n}_{2d}$, and convert the galaxy map to a density contrast map as $\delta = n_{2d}/\bar{n}_{2d} - 1$, where n_{2d} is the galaxy map.

(iii) Then we smooth the density contrast map with a Gaussian filter of comoving scale $\sigma_s = 10$ Mpc h^{-1}.

(iv) We take this smoothed contrast map and consider only the most underdense pixels (with $\delta < \delta_m = -0.3$) as potential void centres. We define the most underdense pixel in the map as the first void centre.

(v) Next, we start defining circular shells of increasing radius around that centre, stopping when the mean density within the slice ($\delta = 0$) is reached. That is, starting with a shell of radius R_v^i, we measure the average galaxy density in the shell $\delta(R_v^i)$, and if the density is negative, we check the next larger shell $\delta(R_v^{i+1})$, where the increment between shells is 1 Mpc h^{-1} in radius. For some shell R_v^j, the density contrast reaches zero, $\delta(R_v^j) \geq 0$, and at that point, the void radius is defined as $R_v = R_v^j$ (see Fig. 1 for a graphical explanation).

(vi) Then all pixels contained in this void are removed from the list of potential void centres, preventing any of these pixels to become the centre of any other void. From the remaining pixels which satisfy $\delta < \delta_m = -0.3$, we define the next most underdense pixel as the second void centre. The process is repeated until all pixels with $\delta < \delta_m = -0.3$ have been assigned to a void.

Beyond the dependence on the LOS size of the projected slice in which the finder is executed, studied in more detail later in this section, the void catalogue produced by this algorithm depends on two parameters: the smoothing scale, σ_s, and the maximum density contrast of a pixel to become a void centre, δ_m. The smoothing scale ($\sigma_s = 10$ Mpc h^{-1}) is chosen to be about half the radius of the smallest voids we can access in our data sample (because of photo-z smearing), and increasing it would erase the structure leading to some of these smallest voids, leaving the large voids intact. On the other hand, the most significant voids found by the algorithm, the deepest ones, are independent of the choice $\delta_m = -0.3$ since their void centre pixel is more underdense than that. By changing the value of δ_m, we are only affecting the shallower voids of the sample. The impact of the δ_m choice is studied in Appendix A. Also, voids found by this algorithm can overlap or even enclose one another, but just in the case where a subvoid is deeper than the bigger void enclosing it.

The process detailed above will produce a list of voids for a given redshift slice. Before describing how various slices are combined to obtain the full void catalogue, we first study the performance of the single slice results in simulations.

3.2 Performance on simulations

In order to validate the performance of the algorithm, we use the simulations, where we have both spectroscopic and photometric redshifts for void tracer galaxies, and we compare the voids found by the algorithm in spec-z and photo-z spaces. In particular, we run the void-finding algorithm twice on each redshift slice: first, using spectroscopic redshifts for selecting the galaxies which go into the slice and then using photometric redshifts which mimic the ones we have in real DES data.

Once we have the spec-z and photo-z defined void catalogues, we measure the projected galaxy density profiles of the voids in them in radial annuli using the true redshifts. Fig. 2 shows the resulting density profiles for both cases in different slice comoving thicknesses. As expected, the void finder performs poorly if the size of the projected slice is smaller or similar to the photo-z dispersion $\sigma_z \simeq 50$ Mpc h^{-1}. Therefore, the accuracy of the finder is a function of the thickness of the projected slice: for slice width $\sim$2 times the size of the typical photometric redshift scatter, the difference between the average density profiles of voids found in spec-z and photo-z is not significant, being smaller than the standard deviation of the stacked void profiles.

Fig. 2 shows that voids found by the algorithm in photo-z space can indeed have very similar density profiles as voids found in spec-z space. However, it is also important to know the relative number of voids found in the two cases. Photometric redshifts produce a smearing in the LOS position of tracers which can actually erase some of the structure, especially on scales comparable to the size of the photo-z scatter or smaller. That will have the consequence of some small voids not being detected in the photo-z case. The voids of size larger than the photo-z scatter should be detected in both cases. Fig. 3 shows the distribution of void radii in simulations for spec-z and photo-z samples. As expected, we find less voids in the
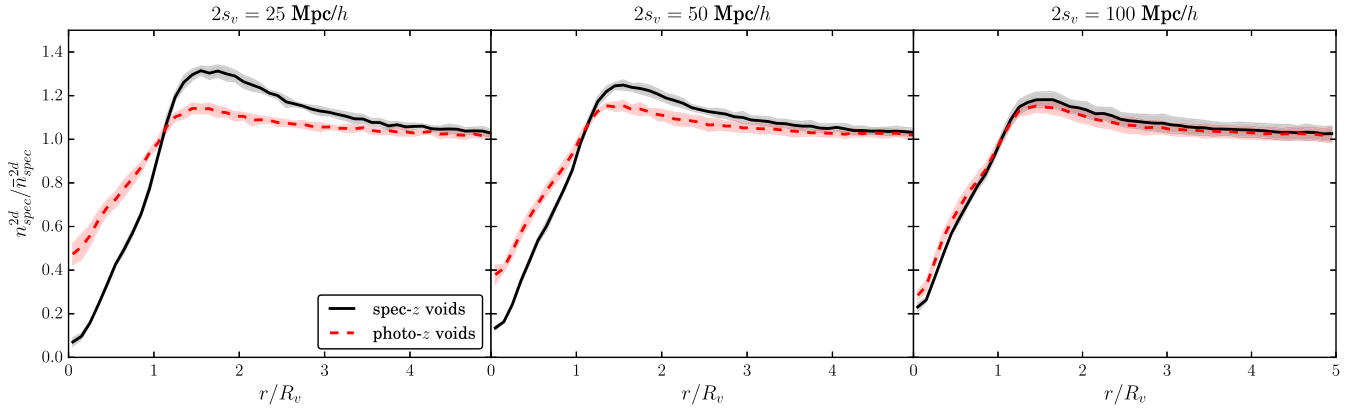
Figure 2. Left-hand panel: comparison of 2D spectroscopic galaxy density profiles of voids found in the simulations using galaxy spectroscopic redshifts (solid line) or photometric redshifts (dotted, red). The shaded regions show the corresponding error bars computed as the standard deviation among all the stacked voids. The projected 2D slice width is 25 Mpc h^{-1}(comoving distance), a scale corresponding to ~1/2 the photometric redshift scatter. For this thin slice, the galaxy density profile is damped significantly by photo-z scatter, making the galaxy profile of photo-z defined voids more shallow. Centre panel: the same, but for a thicker slice of width 50 Mpc h^{-1}, comparable to the photo-z scatter. Right-hand panel: the same, but for a projected slice of width 100 Mpc h^{-1}, twice the size of the typical photo-z scatter. In this case, there is a good match between the profiles of spec-z and photo-z selected voids. For such a thick slice, the fraction of galaxies which are placed in the incorrect slice due to photometric redshift scatter is smaller, allowing accurate void identification from the smoothed galaxy field.
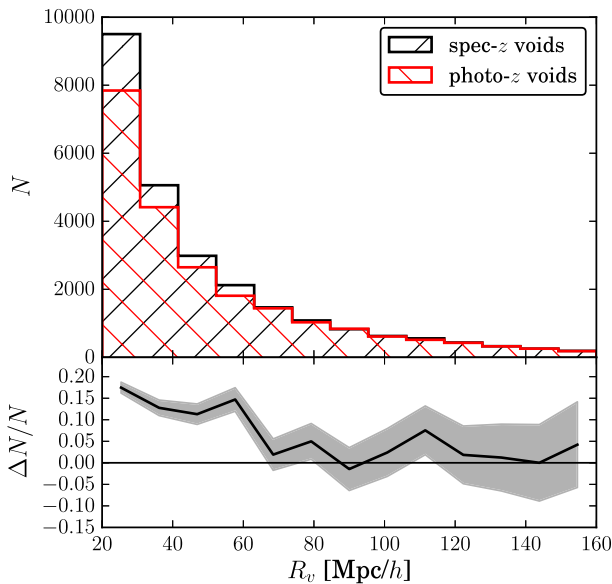
Figure 3. Upper panel: void radius distribution for voids found in spec-z and photo-z simulated galaxy samples, for a slice thickness of $2s_v = 100$ Mpc h^{-1}. Lower panel: relative difference between the distributions (with respect to the spectroscopic redshift case). Some voids with size smaller than the photo-z scatter ($\sigma_z \simeq 50$ Mpc h^{-1}) are smeared out due to photo-z scatter and not detected, resulting in a smaller number of voids relative to the spectroscopic case. For large voids, this effect is not important and the two distributions agree within errors.

photo-z case, with the difference being more important for small voids and becoming negligible for the voids substantially larger than the photo-z dispersion ($\sigma_z \simeq 50$ Mpc h^{-1}).

In addition to the comparison of the galaxy density profiles of voids, which is the most important test of the algorithm, Fig. 4 shows a visual comparison between the positions and radius of spec-z and photo-z defined voids in a random 100 Mpc h^{-1}-thick slice of our simulations. The correlation between the two sets of voids is very clear, in both positions and radii. In some cases, especially for the biggest voids, the match between spec-z and photo-z voids is almost
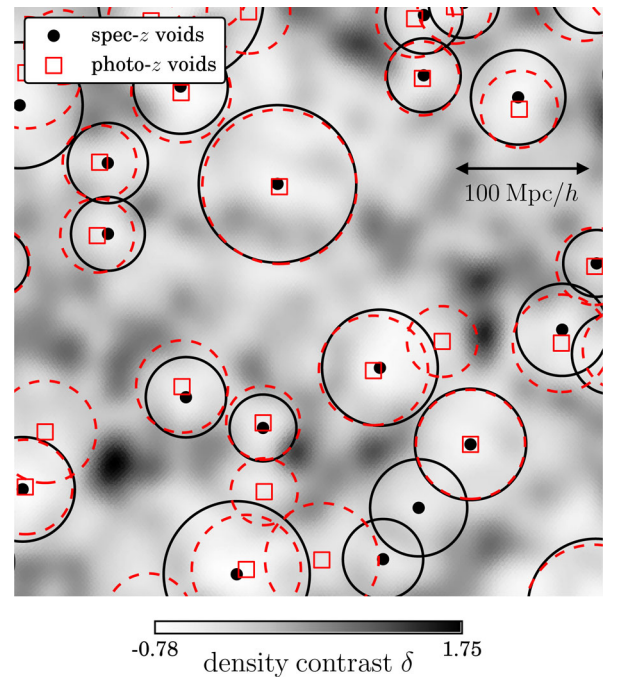

Figure 4. Comparison between voids found in spec-z (centres: filled black points; radius: filled circles) and photo-z (centres: open red squares; radius: red dashed circles) in the simulations for a slice of thickness $2s_v = 100$ Mpc h^{-1}. The background grey-scaled field is the smoothed galaxy field ($\sigma = 10$ Mpc h^{-1}) used by the void-finder. The correlation between spec-z and photo-z defined voids is clear: in many cases, the void position and radius match almost exactly.

perfect. This is remarkable given the magnitude of the scatter in the LOS direction being added by photometric redshifts.

4 DES-SV VOID CATALOGUE

In the previous section, we have presented a void finder which works by projecting galaxies into redshift slices (see Section 3.1
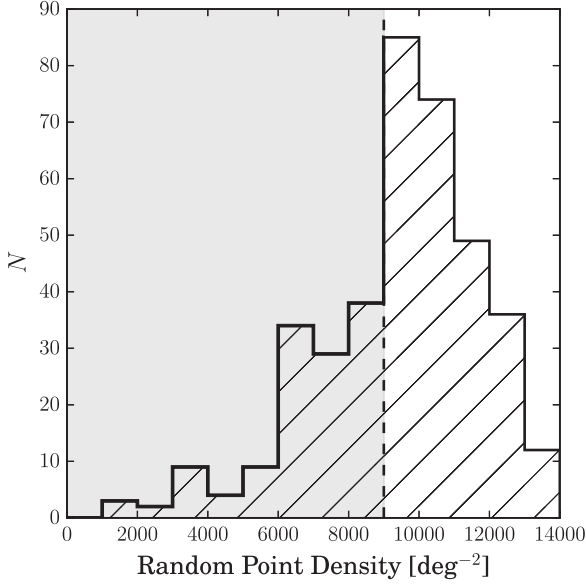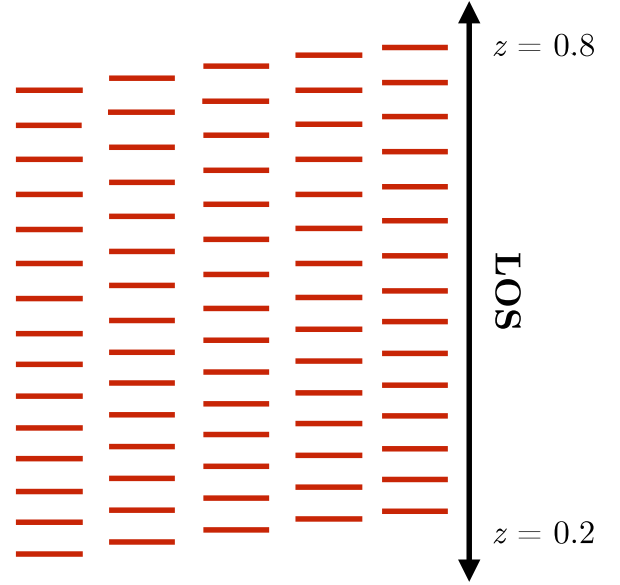
Figure 5. Distribution of random point density inside DES-SV voids, where the random points are distributed uniformly through the DES-SV area. The distribution shows roughly a Gaussian shape at high densities corresponding to voids inside the survey mask, and a low-density tail corresponding to edge voids. We remove all voids with random point density less than 9000 points deg^{-2} (shaded region), and most of them are near the survey edge. This cut removes 33 per cent of the total number of voids.


Figure 6. Graphical representation of the LOS slicing performed in this paper. The black vertical arrow represents the redshift range, $0.2 < z < 0.8$, and the red horizontal bars represent the boundaries of the redshift slices in which the void finder is run. As the diagram shows, we oversample the LOS with slices of thickness 100 Mpc h^{-1} every 20 Mpc h^{-1}. In Fig. 7, we show the way voids in adjacent slices are combined to form the final catalogue.

for a detailed description and parameters used in the algorithm). We have shown (Section 3.2) that as long as the thickness of the projected slice is large enough compared to the photo-z scatter, using photometric redshifts for the position of void tracers works nearly as well as using spectroscopic redshifts. Nevertheless, the algorithm will find some voids which are not likely to correspond to voids in the dark matter density field. Such false voids may be due to a number of effects: (i) at the survey edge or masked areas, we have no information on galaxy positions and (ii) duplicate voids may appear if slices overlap in redshift. In this section, we apply the algorithm to real DES-SV data, and present the way we deal with voids near the survey edge (Section 4.1) and the strategy we follow to get the most of the LOS information in the data (Section 4.2). The properties of the final DES-SV void catalogue are presented in Section 4.3.

4.1 Voids near the survey edge

The assignment of each void's radius does not distinguish between voids which are fully contained within the survey and those which extend beyond it. The void radius may stretch beyond the edge of the survey, into areas which may or may not correspond to voids in the galaxy distribution. To remove such voids which extend far beyond the survey edge, we use the method of Clampitt & Jain (2015). A random point catalogue drawn using the survey mask is generated, and for each void, we calculate the density of random points inside R_v. The distribution of random points density inside voids is shown in Fig. 5, and it presents a Gaussian-like shape at high densities (peaked around 9500 points deg^{-2} with $\sigma \simeq 2000$ points deg^{-2}), corresponding to voids centred in the survey mask, and a low density tail reaching almost zero density, which corresponds to edge voids. Due to the small size of the DES-SV patch used in this work, with an area of 139 deg^2, and the size of some of the voids detected (a void with $R_v \sim 80$ Mpc h^{-1} would span more than 10°

in diameter at $z = 0.3$), we place a conservative cut and discard voids with random point density less than 9000 points deg^{-2}, which constitute 33 per cent of the total number of voids.

4.2 LOS slicing strategy

To obtain more information about the LOS position of each void, we oversample the volume with a number of different slice centres. In particular, first we slice the LOS range of the survey, $0.2 < z < 0.8$, in equal slices of comoving thickness $2s_v = 100$ Mpc h^{-1} taking the upper redshift limit, $z = 0.8$, as the upper limit of the furthest slice. Then, we apply a shift to this slicing of 20 Mpc h^{-1} towards low redshift, and we repeat the process four times so that we have a slice of thickness 100 Mpc h^{-1} centred every 20 Mpc h^{-1} of the LOS range in the data (see Fig. 6 for a graphical representation).

Since the volume has been oversampled with a number of different slice centres, sometimes, the same physical void will be found in multiple slices, creating elongated void structures in the LOS (left-hand panel in Fig. 7). Each of these structures may actually correspond to one physical underdensity, or at least their void candidate members will have a consistent lensing profile since they are essentially at the same redshift and have very similar sizes. In order to remove the duplicate voids, and also to pick up the right void centre in the LOS direction, we need to group these void structures together. The groups are found by joining voids in neighbouring (and hence overlapping) slices which have a small angular separation between them. In particular, two voids with radii R_v^i and R_v^j and found in neighbouring slices will become part of the same group if the angular distance between their centres is smaller than half the mean angular radii of the two voids: $\bar{R}_v/2 = (R_v^i + R_v^j)/4$. The groups are shown in the central panel in Fig. 7, and the right-hand panel shows the final void catalogue, without obvious elongated structures in the LOS. This resulting void catalogue is not very sensitive to the choice of $\bar{R}_v/2$: Increasing this minimum
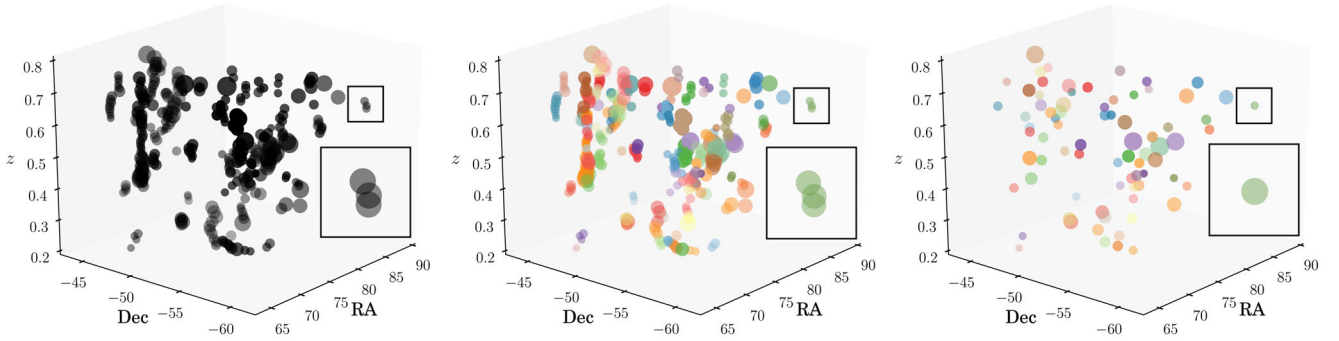
Figure 7. Left-hand panel: 3D position of voids found in the slicing shown in Fig. 6. Each void candidate is shown as a sphere with size proportional to the void radius. Due to oversampling in the LOS, slices overlap and duplicates of the same physical void are found in different slices, apparent in this plot as elongated structures in redshift. The inset square shows the case of a three-void group. Centre panel: voids corresponding to the same physical underdensity are grouped together (as described in Section 4.2) and plotted with a common colour. Right-hand panel: the final void positions are computed as the median 3D position of the members of each group.

separation from $0.5\bar{R}_v$ to $0.6\bar{R}_v$ ($0.8\bar{R}_v$) results in removing 6 per cent (10 per cent) of the voids in the final catalogue.

Once we have the void groups corresponding to those LOS structures, we compute the 3D position of each group (RA, Dec and redshift) as the median position of the different void members of the group. The relative scatter in this determination inside each group (taken as the standard deviation of each quantity with respect to its mean value) is very small (less than 0.4 per cent for RA and Dec and around 2 per cent in redshift). The void radius is also computed as the median void radius of the different void members in each group, with a relative scatter around 14 per cent. The final void candidates, after removal of duplications of potential physical underdensities due to the oversampled slicing, are shown in the right-hand panel of Fig. 7. The effect of the LOS slicing strategy in the void lensing measurement is tested in Appendix B, where we show it helps reduce the noise but it does not affect the main outcomes from the measurement.
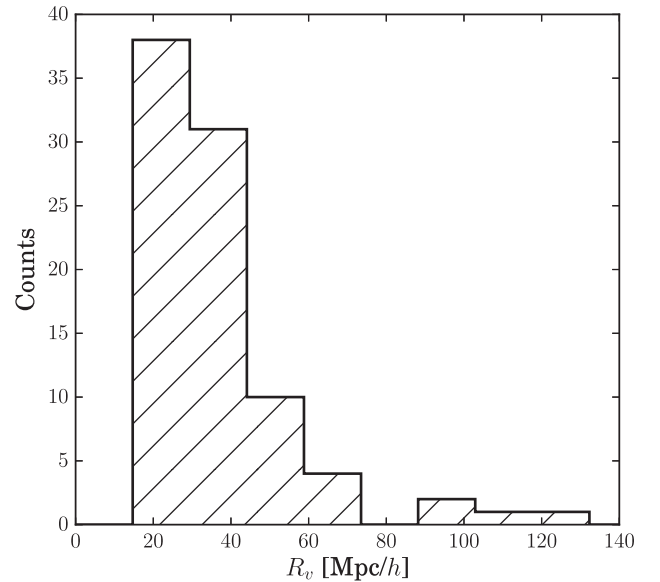
4.3 Final void catalogue

Applying the void-finding algorithm described in Section 3, using slices of 100 Mpc h^{-1} thickness, to the DES-SV redMaGiC catalogue, and after making the cuts presented in Sections 4.1 and 4.2, we find a total of 87 voids in the 139 deg^2 of survey area. These voids are identified in the redshift range $0.2 < z < 0.8$, and they have comoving sizes ranging from $R_v = 18$ Mpc h^{-1} to $R_v = 120$ Mpc h^{-1}, with a mean void radius of $\bar{R}_v = 37$ Mpc h^{-1}. Fig. 8 shows the full void radius distribution for the sample. The mean angular radius of voids in the sky is 1°.5, while their mean redshift is $\bar{z} = 0.57$.

Fig. 9 shows the 2D galaxy density profiles of voids found in the DES-SV data and in simulations, using galaxy photometric redshifts. The agreement between data and simulations is good, and so is the agreement between the simulation profiles measured with photometric (Fig. 9) and spectroscopic redshifts (*right-hand panel* of Fig. 2).

5 VOID LENSING

Using the void catalogue defined in the previous section, we now focus on the lensing measurement around voids. This represents a key result, since a significant lensing signal around voids proves them to be underdense in the matter field, this way demonstrating the

Figure 8. Distribution of comoving void radii of the final DES-SV void catalogue used in this work, using slices of thickness 100 Mpc h^{-1} and after the cuts described in Sections 4.1 and 4.2.

void catalogue is primarily composed of real underdensities rather than spurious detections, tracer density effects or any systematics in the data.

In this section, we present the details of the lensing measurement and covariance, the results for the tangential and cross-components of that measurement and their significance, and the fit of the tangential component to a void model widely used in the literature.
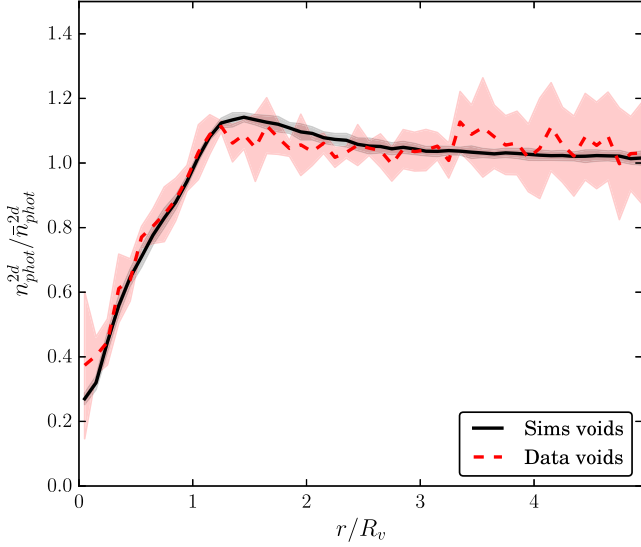
5.1 Measurement

Assuming an axisymmetric density profile, the stacked excess surface mass density $\Delta\Sigma$ is related to the tangential shear γ_t of source galaxies by

$$\Delta\Sigma(R/R_v) = \Sigma_{\text{crit}}\gamma_t(R/R_v), \tag{1}$$

where the proportionality factor describing the lensing strength is

$$\Sigma_{\text{crit}}(z_L, z_s) = \frac{c^2}{4\pi G}\frac{D_A(z_s)(1+z_L)^{-2}}{D_A(z_L)D_A(z_L, z_s)}, \tag{2}$$

Figure 9. Comparison of 2D galaxy density profiles of voids found in DES-SV data and simulations, using galaxy photometric redshifts. The shaded regions show the corresponding error bars computed as the standard deviation among all the stacked voids.

with $\Sigma_{\mathrm{crit}}^{-1}(z_{\mathrm{L}}, z_{\mathrm{s}}) = 0$ for $z_{\mathrm{s}} < z_{\mathrm{L}}$, where z_{L} and z_{s} are the lens and source galaxy redshifts, respectively. Note both the use of comoving units and that we need to assume a certain cosmology (flat ΛCDM with $\Omega_{\mathrm{m}} = 0.3$) when calculating the angular diameter distances D_A in Σ_{crit}. Our lensing projected surface density estimator is therefore given by

$$\Delta\Sigma_k(R/R_v; z_{\mathrm{L}}) = \frac{\sum_j \left[w_j \gamma_{k,j}(R/R_v)\Sigma_{\mathrm{crit},j}(z_{\mathrm{L}}, z_{\mathrm{s}}) \right]}{\sum_j w_j} \qquad (3)$$

where k denotes the two possible components of the shear (tangential and cross), the summation $\sum_j$ runs over all the source galaxies in the radial bin R/R_v, around every void position, and the optimal weight for the jth galaxy is given by (Sheldon et al. 2004):

$$w_j = \frac{[\Sigma_{\mathrm{crit},j}^{-1}(z_{\mathrm{L}}, z_{\mathrm{s}})]^2}{\sigma_{\mathrm{shape}}^2 + \sigma_{\mathrm{m},j}^2} . \qquad (4)$$

Here, σ_{shape} is the intrinsic shape noise (SN) for each source galaxy, and $\sigma_{\mathrm{m},j}$ is the shape measurement error. In Section 5.5, we relate the differential surface density $\Delta\Sigma$ to the 3D void profile ρ_{v}.

Note that since the projected void radius R_v ranges from 20 to more than 100 Mpc h^{-1}, we stack the measured shear profiles in units of the void radius, R/R_v. Stacking the profiles in physical distance would smooth out the stacked void density profiles and hence some of the signal would be lost.

5.2 Covariance

In order to estimate the covariance for the $\Delta\Sigma(R)$ measurements in this work, we combine two different approaches: we rely on the jackknife (JK) method to estimate the signal variance while we estimate the off-diagonal shape of the covariance from the lensing SN of the measurement (Melchior et al. 2014). The main reason for that combination is the limitation in the JK technique due to the small number of voids ($\sim$100) in our catalogue, yielding very noisy off-diagonal correlations. However, we can obtain smooth SN-only covariances by applying any number of random rotations

to the ellipticities of source galaxies. Next, we explain the precise combination of the two approaches.

Due to the small number of voids in the DES-SV catalogue, we perform a void-by-void jackknife: we carry out the measurement multiple times with each void omitted in turn to make as many jackknife realizations as voids we have in the sample (N). Then, the variance of the measurement (Norberg et al. 2009) is given by

$$\sigma_{\mathrm{JK}}^2(\Delta\Sigma_i) = \frac{(N-1)}{N} \times \sum_{\mathrm{JK}-k=1}^{N} \left[(\Delta\Sigma_i)^{\mathrm{JK}-k} - \overline{\Delta\Sigma_i} \right]^2 \qquad (5)$$

where the mean value is

$$\overline{\Delta\Sigma_i} = \frac{1}{N} \sum_{\mathrm{JK}-k=1}^{N} (\Delta\Sigma_i)^{\mathrm{JK}-k} , \qquad (6)$$

and $(\Delta\Sigma_i)^{\mathrm{JK}-k}$ denotes the measurement from the kth JK realization and the ith spatial bin.

The SN covariance of the measurement is estimated by randomly rotating the orientation of each source galaxy ellipticity many times ($N_{\mathrm{SN}} = 300$ in this analysis) and repeating the $\Delta\Sigma$ lensing measurement each time. Then the covariance is estimated as

$$\mathrm{Cov}_{\mathrm{SN}}[\Delta\Sigma_i, \Delta\Sigma_j] = \frac{1}{N_{\mathrm{SN}}}$$
$$\times \sum_{\mathrm{SN}-k=1}^{N_{\mathrm{SN}}} \left[(\Delta\Sigma_i)^{\mathrm{SN}-k} - \overline{\Delta\Sigma_i} \right] \left[(\Delta\Sigma_j)^{\mathrm{SN}-k} - \overline{\Delta\Sigma_j} \right] \qquad (7)$$

where the mean value is

$$\overline{\Delta\Sigma_i} = \frac{1}{N} \sum_{\mathrm{SN}-k=1}^{N} (\Delta\Sigma_i)^{\mathrm{SN}-k} , \qquad (8)$$

and $(\Delta\Sigma_i)^{\mathrm{SN}-k}$ denotes the measurement from the kth SN realization and the ith spatial bin.

Fig. 10 shows a comparison of the measurement variance estimated from jackknife and SN, following the techniques described above. The errors coming from the two approaches agree well on the smallest scales, as expected since the small-scale regime is dominated by SN. However, at mid to large scales ($R \sim 0.28R_v$ and above), the JK errors get bigger than SN only, as they can trace other effects such as systematics in the data or sample variance. The SN calculation is, on the other hand, more adequate for off-diagonal elements of the covariance since it avoids the intrinsic noise limitation of the JK technique. Hence, in order to have a smooth covariance matrix with variance accurately estimated from JK, we follow the approach of fixing the shape of the covariance as given by the SN calculation, and renormalize it to the JK estimates of the variance:

$$\mathrm{Cov}[\Delta\Sigma_i, \Delta\Sigma_j] = \mathrm{Corr}_{\mathrm{SN}}[\Delta\Sigma_i, \Delta\Sigma_j]\sigma_{\mathrm{JK}}(\Delta\Sigma_i)\sigma_{\mathrm{JK}}(\Delta\Sigma_j) \qquad (9)$$

where $\mathrm{Corr}_{\mathrm{SN}}[\Delta\Sigma_i, \Delta\Sigma_j]$ is the SN correlation matrix (or reduced covariance) given by

$$\mathrm{Corr}_{\mathrm{SN}}[\Delta\Sigma_i, \Delta\Sigma_j] = \frac{\mathrm{Cov}_{\mathrm{SN}}[\Delta\Sigma_i, \Delta\Sigma_j]}{\sigma_{\mathrm{SN}}(\Delta\Sigma_i)\sigma_{\mathrm{SN}}(\Delta\Sigma_j)} \qquad (10)$$

The approach of renormalizing a smooth covariance to a JK-estimated variance has been used before in the literature, for example by Crocce et al. (2016).

5.3 Null tests: cross-component and *randomized* voids

The cross-component of the measurement described in Section 5.1 is not produced by gravitational lensing and therefore is expected
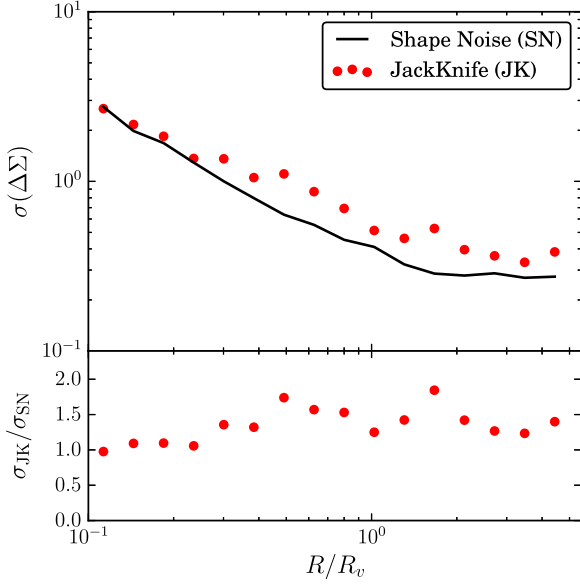
Figure 10. Upper panel: variance in the stacked weak lensing measurement of voids in DES-SV data, in bins of R/R_v, as estimated from JK resampling and lensing SN, the two techniques described in Section 5.2. Lower panel: ratio of the two error estimations in the upper panel. The two agree well on small scales (which are SN dominated) and differ significantly at medium to large scales since the jackknife includes other sources of variance in addition to SN.
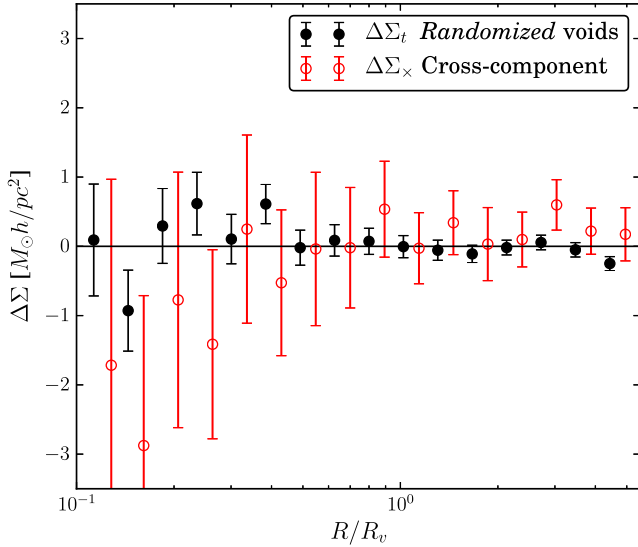
Figure 11. Cross-component of the DES-SV data stacked lensing measurement for true voids and tangential component for the lensing around randomized voids, in bins of R/R_v. Both measurements are compatible with the null hypothesis with $\chi^2_{\rm null}/{\rm dof} = 8.2/16$ and $\chi^2_{\rm null}/{\rm dof} = 18.7/16$, respectively. The error using randomized voids is smaller since the measurement involves ~10 times more randomized voids.

to vanish at first order. Similarly, the tangential component of the same measurement around *randomized* voids, which follow the size and redshift distribution of true voids but are randomly distributed in the survey area (Appendix C), is also expected to vanish. Fig. 11 shows the cross-component of the stacked lensing measurement for true voids and the tangential component for *randomized* voids.
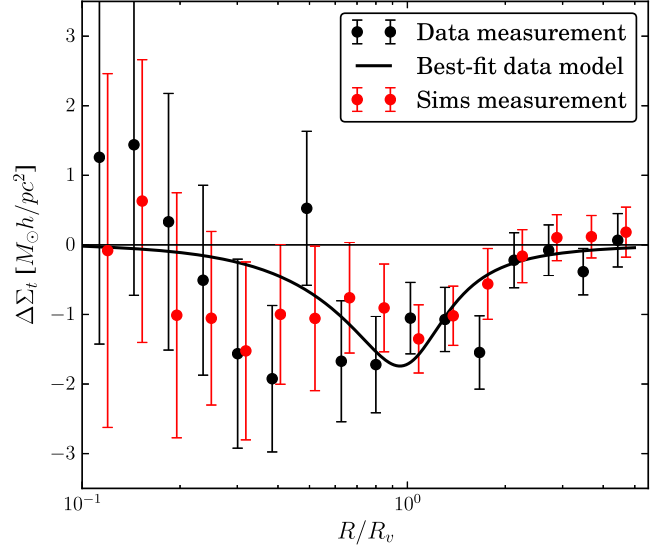
Figure 12. Stacked tangential shear profile around voids in DES-SV data (black points) and simulations (red points) in bins of R/R_v. The black solid line shows the best-fitting model (see Section 5.5) to the data shear signal. The χ^2 for the null hypothesis in the data measurement is $\chi^2_{\rm null}/{\rm dof} = 35.5/16$, yielding an estimated S/N = 4.4, while the theory model provides a good fit to the data with $\chi^2/{\rm dof}=13.2/14$. The measurement in the simulations shows consistency with the data best-fitting model, yielding $\chi^2/{\rm dof}=10.1/14$.

With dof $= N_{\rm bin}$ as the number of R/R_v bins in the measurement and no model parameters, the null hypothesis χ^2 can be computed as

$$\chi^2_{\rm null} = \sum_{i,j} \Delta\Sigma_i {\rm Cov}^{-1}_{ij} \Delta\Sigma_j \qquad (11)$$

where i, j correspond to radial bins in $\Delta\Sigma$ and Cov is the covariance matrix.

The cross-component of the measurement yields a $\chi^2_{\rm null}/{\rm dof} = 8.2/16$, and the tangential measurement around *randomized* voids, which are 10 times more numerous than true voids and whose production is described in greater detail in Appendix C, yields a $\chi^2_{\rm null}/{\rm dof} = 18.7/16$, both showing consistency with the null hypothesis.

5.4 Tangential shear profile

Fig. 12 shows the measurement of the tangential component of the stacked lensing signal around voids. Assuming a non-central χ^2 distribution, we can compute the signal-to-noise (S/N) of the measurement as

$$({\rm S/N})^2 = \chi^2_{\rm null} - {\rm dof} = \sum_{i,j} \Delta\Sigma_i {\rm Cov}^{-1}_{ij} \Delta\Sigma_j - N_{\rm bin} \qquad (12)$$

The evaluation of this expression yields $\chi^2/{\rm dof} = 35.5/16$ and hence S/N = 4.4. The significance of the signal is complemented with the null tests in the previous subsection being consistent with the null hypothesis. Furthermore, we test the robustness of the signal to changes in the LOS slicing strategy in Appendix B and to changes in the value of δ_m in Appendix A.
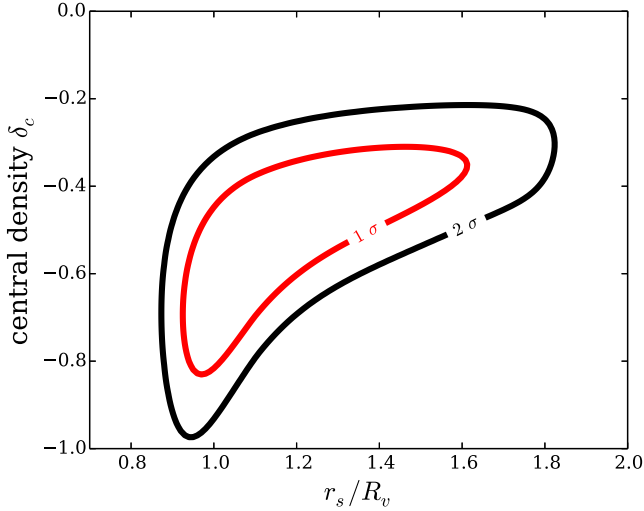
Figure 13. Constraints on void central underdensity δ_c and scale radius r_s from the DES-SV data void lensing measurements in Fig. 12. Best-fitting values are $r_s = 1.05 R_v$ and $\delta_c = -0.60$, and the χ^2/dof for the fit is 13.2/14. There is good agreement between the void edge determined from galaxies, R_v, and the void edge determined from lensing, r_s.

5.5 Model fits

We use the 3D void profile of Hamaus, Sutter & Wandelt (2014b) (henceforth HSW14)

$$\frac{\rho_v(r)}{\bar{\rho}} - 1 = \delta_c \frac{1 - (r/r_s)^\alpha}{1 + (r/R_v)^\beta}, \tag{13}$$

and fit two parameters: the central underdensity δ_c and the scale radius r_s. Note that r here denotes the 3D (in contrast to projected) radius. We do not fit the inner and outer slopes α and β using the lensing data, but fix their values to the simulation fits of HSW14. That work showed that α and β are not independent parameters but determined by the ratio r_s/R_v, which yields $\alpha = 2.1$ and $\beta = 9.1$ for the best-fitting r_s shown in Fig. 13. Following Krause et al. (2013), the lensing observable $\Delta\Sigma(R/R_v)$ is related to the 3D density by

$$\Delta\Sigma(R/R_v) = \bar{\Sigma}(< R/R_v) - \Sigma(R/R_v), \tag{14}$$

where the projected surface density is given by

$$\Sigma(R/R_v) = \int \mathrm{d}r_{\text{los}}\, \rho_v\left(\sqrt{r_{\text{los}}^2 + R^2}\right) - \bar{\rho}, \tag{15}$$

and $\bar{\rho}$ is the cosmological mean mass density.

The resulting parameter constraints are shown in Fig. 13. The reduced $\chi^2/\text{dof} = 13.2/14$ implies a good fit to the theory model. Even though the uncertainties are important, the best-fitting $\delta_c = -0.60$ is in agreement with the density profile shown in Fig. 9, which is at the same time in agreement with the profile measured in simulations. In order to further support the data measurement using simulations, we have measured the lensing signal in the simulations using the same number of voids as in the data. The resulting measurement can be found in Fig. 12, and it shows consistency with the best-fitting model to the data with $\chi^2/\text{dof} = 10.1/14$.

Additionally, the best-fitting δ_c and the trend in Fig. 13 are in agreement with findings in HSW14. However, note the important differences between our work and HSW14: we use photometric galaxies instead of *N*-body dark matter particles. More importantly, we are using a different void finder. Thus, it should not be surprising

that our mean void radius (R_v), scale radius (r_s), and mean void underdensity (δ_c) do not match all the relations obeyed by theirs. For example, their void sample with $r_s/R_v \simeq 1.05$ (matching our best-fitting value) is slightly smaller ($R_v \simeq 29$ Mpc h^{-1}) and more empty ($\delta_c \simeq -0.7$) than ours.

Finally, we can use the constraints on δ_c being negative as an alternative estimate of the significance in the lensing detection, which is consistent with the estimation in equation (12): marginalizing over r_s, we find $\delta_c < 0$ with a significance of 4.6σ (4.8σ if we fix r_s to its best-fitting value). The best-fitting value of r_s is compatible with R_v at the 1σ level. Based on equation (13), $r = r_s$ is just the place where the local 3D density returns to the cosmic mean, $\rho = \bar{\rho}$. The definition of R_v is based on where the local galaxy density returns to the mean (Fig. 1). So given this best-fitting model, we see that the void wall in the mass distribution (determined from lensing) agrees well with the void wall in the galaxy distribution.

5.6 Comparison to previous measurements

Other measurements of weak gravitational lensing around voids or underdensities have been performed in recent years. Melchior et al. (2014) used the SDSS void catalogue of Sutter et al. (2012) to carry out the first detection of lensing around voids, although at low S/N. Clampitt & Jain (2015), using a similar data sample, optimized the void-finding strategy for lensing purposes and were able to achieve a higher S/N ~ 7 in the lensing measurement. The void finder in this work is similar to that of Clampitt & Jain (2015), even though we did not attempt to optimize the lensing detection but to minimize the photo-*z* related impact in the void-finding procedure. Our comparable lensing S/N is encouraging given the use of photometric redshifts and a smaller data set – this highlights the viability of photometric void finders as well as the quality of the DES data.

Gruen et al. (2016) changed the approach and, instead of looking at individual cosmic voids, measured the lensing signal around troughs in the DES-SV galaxy distribution, defined as underdensities in the projection of lens galaxies over a wide range in redshift. That produced a high S/N lensing measurement around those structures, and they successfully modelled that to probe the connection between galaxies and matter. In that respect, trough lensing does not constrain void profiles or abundances but it is sensitive to the galaxy bias and even cosmology.

6 DISCUSSION

We have presented a new void finder designed for photometric surveys and applied it to early Dark Energy Survey data and simulations. Fixing the LOS size of the slice to be at least twice the photo-*z* scatter, we find the number of voids found in simulated spectroscopic and photometric galaxy catalogues to be within 20 per cent for all transverse void sizes, and indistinguishable for voids with projected size larger than 70 Mpc h^{-1}. For such large voids, most have a one-to-one match with nearly the same assigned centre and radius.

This result – that the largest voids are the ones most faithfully preserved in a photometric redshift survey – has implications for the expected spatial and dynamic properties of our voids. Ceccarelli et al. (2013) classified voids into those with and without surrounding overdense shells: large voids without shells tend to expand, while smaller voids surrounded by overdense shells are in the process of being crushed by the surrounding shell. This is a useful division for understanding void dynamics, as predicted analytically by

Sheth & van de Weygaert (2004) and later studied in simulations (Ceccarelli et al. 2013; Paz et al. 2013; Hamaus et al. 2014b) and data (Ruiz et al. 2015). Furthermore, this classification has been useful for predicting large-scale bulk flows of voids in both simulations (Lambas et al. 2016) and data (Ceccarelli et al. 2016). These works found that large voids are on average receding from each other, while small voids in overdense shells are approaching each other.

Most importantly, we have applied the algorithm to the DES-SV data and found a total of 87 voids over the redshift range $0.2 < z < 0.8$. Our $\sim 4\sigma$ detection of the weak gravitational lensing signal of these voids shows they are truly underdense in the matter field and hence not simply a product of Poisson noise, tracer density effects or any systematics in the data. Assuming a model profile (HSW14), we find a best-fitting central density of $\delta_c \sim -0.6$ and scale radius $r_s \sim R_v$. Since r_s is the void edge determined from lensing, and R_v is the edge determined from the galaxy distribution, the best-fitting lensing model shows consistency between the mass and galaxy distributions of voids. Note however that the contours are broad and still allow for the possibility of $r_s \gtrsim R_v$.

Further applications of the same void finder will be explored in future DES data samples. Of particular interest is the study of the CMB cold imprint of voids (Kovács et al. 2016), related to the properties and presence of Dark Energy through the integrated Sachs–Wolfe effect (Granett et al. 2008; Cai et al. 2010; Cai, Padilla & Li 2014; Hotchkiss et al. 2014).

The advances in this work towards finding voids in photometric surveys are also exciting in light of recent advances in void cosmology. Clampitt et al. (2016a) studied void–void and void–galaxy clustering and derived void bias, using the spectroscopic SDSS LRG sample. Hamaus et al. (2016) applied the Alcock–Paczynski test to void clustering statistics to put ~ 10 per cent constraints on Ω_m using voids identified using CMASS galaxies as tracers, a result that was anticipated in simulations by the same group (Hamaus et al. 2014c,a, 2015). Kitaura et al. (2016) reported greater than 3σ evidence of the presence of baryonic acoustic oscillations (BAO) in void correlations, again using CMASS galaxies. This impressive measurement was made possible by the new void finder presented in Zhao et al. (2016) and detailed studies with mock CMASS samples presented in Liang et al. (2016). While the CMASS sample from BOSS covers a very large area, it lacks a suitable background source sample for direct lensing measurements of void density profiles. Upcoming photometric surveys, which will have many background sources available, will make the combination of void clustering and lensing over large volumes a reality.

In addition to constraining standard cosmological parameters, voids have been used to investigate alternative dark matter scenarios like warm dark matter (Yang et al. 2015), or the effects of neutrinos on void lensing (Massara et al. 2015). Especially numerous are the studies on void abundance (Li 2011; Clampitt, Cai & Li 2013; Cai et al. 2015; Lam et al. 2015; Zivick et al. 2015; Pollina et al. 2016) and lensing (Cai et al. 2014; Barreira et al. 2015) as promising probes of alternatives to general relativity (GR). In particular, Barreira et al. (2015) used simulations of Galileon gravity to show that the lensing signal of voids can be double that in GR. Comparing to the SDSS void lensing results of Clampitt & Jain (2015), they showed that the size of the difference is comparable to current observational errors. Furthermore, another recent development by Cautun, Cai & Frenk (2016) has shown that the signal-to-noise ratio for void lensing can be increased by describing the void profile relative to the boundary rather than the centre. Such advances,

combined with the increasing quality and volume of data from ongoing surveys, will bring modified gravity constraints using voids within reach. The algorithm in this work ensures that the statistical power of these new photometric data sets can be brought to bear on void measurements.

REFERENCES

Aihara H. et al., 2011, ApJS, 193, 29

Barreira A., Cautun M., Li B., Baugh C. M., Pascoli S., 2015, J. Cosmol. Astropart. Phys., 2015, 028

Becker M. R. et al., 2016, Phys. Rev. D, 94, 022002

Behroozi P. S., Wechsler R. H., Wu H.-Y., 2013, ApJ, 762, 109

Betancort-Rijo J., Patiri S. G., Prada F., Romano A. E., 2009, MNRAS, 400, 1835

Bonnett C. et al., 2016, Phys. Rev. D, 94, 042005

Bos E. G. P., van de Weygaert R., Dolag K., Pettorino V., 2012, MNRAS, 426, 440

Bruzual G., Charlot S., 2003, MNRAS, 344, 1000

Busha M. T., Wechsler R. H., Becker M. R., Erickson B., Evrard A. E., 2013, Am. Astron. Soc. Meeting, 221, 341.07

Cai Y.-C., Cole S., Jenkins A., Frenk C. S., 2010, MNRAS, 407, 201

Cai Y.-C., Padilla N., Li B., 2014, preprint (arXiv:1410.8355)

Cai Y.-C., Padilla N., Li B., 2015, MNRAS, 451, 1036

Cautun M., Cai Y.-C., Frenk C. S., 2016, MNRAS, 457, 2540

Ceccarelli L., Padilla N. D., Valotto C., Lambas D. G., 2006, MNRAS, 373, 1440

Ceccarelli L., Paz D., Lares M., Padilla N., Lambas D. G., 2013, MNRAS, 434, 1435

Ceccarelli L., Ruiz A. N., Lares M., Paz D. J., Maldonado V. E., Luparello H. E., Lambas D. G., 2016, MNRAS, 461, 4013

Chan K. C., Hamaus N., Desjacques V., 2014, Phys. Rev. D, 90, 103521

Chang C. et al., 2015, Phys. Rev. Lett., 115, 051301

Clampitt J., Jain B., 2015, MNRAS, 454, 3357

Clampitt J., Cai Y.-C., Li B., 2013, MNRAS, 431, 749

Clampitt J., Jain B., Sánchez C., 2016a, MNRAS, 456, 4425

Clampitt J. et al., 2016b, MNRAS, preprint (arXiv:1603.05790)

Colberg J. M., Sheth R. K., Diaferio A., Gao L., Yoshida N., 2005, MNRAS, 360, 216

Colberg J. M. et al., 2008, MNRAS, 387, 933

Colless M. et al., 2001, MNRAS, 328, 1039

Conroy C., Wechsler R. H., Kravtsov A. V., 2006, ApJ, 647, 201

Crocce M., Pueblas S., Scoccimarro R., 2006, MNRAS, 373, 369

Crocce M., Gaztañaga E., Cabré A., Carnero A., Sánchez E., 2011, MNRAS, 417, 2577

Crocce M. et al., 2016, MNRAS, 455, 4301

Dark Energy Survey Collaboration et al., 2016, MNRAS, 460, 1270

Dawson K. S. et al., 2013, AJ, 145, 10

de Jong J. T. A. et al., 2013, ESO Messenger, 154, 44

Diehl H. T. et al., 2014, Proc. SPIE, 91490V

Drinkwater M. J. et al., 2010, MNRAS, 401, 1429

Elyiv A., Marulli F., Pollina G., Baldi M., Branchini E., Cimatti A., Moscardini L., 2015, MNRAS, 448, 642

Flaugher B., 2005, Int. J. Mod. Phys., A20, 3121

Flaugher B. et al., 2015, AJ, 150, 150

Gorski K. M., Hivon E., Banday A. J., Wandelt B. D., Hansen F. K., Reinecke M., Bartelmann M., 2005, ApJ, 622, 759

Granett B. R., Neyrinck M. C., Szapudi I., 2008, ApJ, 683, L99

Gruen D. et al., 2016, MNRAS, 455, 3367

Hamaus N., Wandelt B. D., Sutter P. M., Lavaux G., Warren M. S., 2014a, Phys. Rev. Lett., 112, 041304

Hamaus N., Sutter P. M., Wandelt B. D., 2014b, Phys. Rev. Lett., 112, 251302 HSW14

Hamaus N., Sutter P., Lavaux G., Wandelt B. D., 2014c, J. Cosmol. Astropart. Phys., 2014, 013

Hamaus N., Sutter P., Lavaux G., Wandelt B. D., 2015, J. Cosmol. Astropart. Phys., 2015, 036

Hamaus N., Pisani A., Sutter P. M., Lavaux G., Escoffier S., Wandelt B. D., Weller J., 2016, Phys. Rev. Lett., 117, 091302

Hotchkiss S., Nadathur S., Gottlober S., Iliev I. T., Knebe A., Watson W. A., Yepes G., 2014, MNRAS, 446, 1321

Hoyle F., Vogeley M. S., 2002, ApJ, 566, 641

Jarvis M. et al., 2016, MNRAS, 460, 2245

Jennings E., Li Y., Hu W., 2013, MNRAS, 434, 2167

Kaiser N., Tonry J. L., Luppino G. A., 2000, PASP, 112, 768

Kitaura F.-S. et al., 2016, Phys. Rev. Lett., 116, 171301

Kovács A. et al., 2016, MNRAS, preprint (arXiv:1610.00637)

Krause E., Chang T.-C., Doré O., Umetsu K., 2013, APJL, 762, 120

Kwan J. et al., 2017, MNRAS, 464, 4045

Lam T. Y., Clampitt J., Cai Y.-C., Li B., 2015, MNRAS, 450, 3319

Lambas D. G., Lares M., Ceccarelli L., Ruiz A. N., Paz D. J., Maldonado V. E., Luparello H. E., 2016, MNRAS, 455, L99

Lavaux G., Wandelt B. D., 2010, MNRAS, 403, 1392

Lavaux G., Wandelt B. D., 2012, ApJ, 754, 109

Le Fèvre O. et al., 2005, A&A, 439, 845

Lee J., Park D., 2009, ApJ, 696, L10

Leistedt B. et al., 2016, ApJS, 226, 24

Lewis A., Bridle S., 2002, Phys. Rev. D, 66, 103511

Li B., 2011, MNRAS, 411, 2615

Liang Y., Zhao C., Chuang C.-H., Kitaura F.-S., Tao C., 2016, MNRAS, 459, 4020

Mao Q., Berlind A. A., Scherrer R. J., Neyrinck M. C., Scoccimarro R., Tinker J. L., McBride C. K., Schneider D. P., 2016, preprint (arXiv:1602.06306)

Massara E., Villaescusa-Navarro F., Viel M., Sutter P., 2015, J. Cosmol. Astropart. Phys., 2015, 018

Melchior P., Sutter P. M., Sheldon E. S., Krause E., Wandelt B. D., 2014, MNRAS, 440, 2922

Nadathur S., Hotchkiss S., Diego J. M., Iliev I. T., Gottlober S., Watson W. A., Yepes G., 2015, MNRAS, 449, 3997

Neyrinck M. C., 2008, MNRAS, 386, 2101

Norberg P., Baugh C. M., Gaztañaga E., Croton D. J., 2009, MNRAS, 396, 19

Padilla N. D., Ceccarelli L., Lambas D. G., 2005, MNRAS, 363, 977

Paz D., Lares M., Ceccarelli L., Padilla N., Lambas D. G., 2013, MNRAS, 436, 3480

Platen E., Van De Weygaert R., Jones B. J. T., 2007, MNRAS, 380, 551

Pollina G., Baldi M., Marulli F., Moscardini L., 2016, MNRAS, 455, 3075

Reddick R. M., Wechsler R. H., Tinker J. L., Behroozi P. S., 2013, ApJ, 771, 30

Rozo E. et al., 2016, MNRAS, 461, 1431

Ruiz A. N., Paz D. J., Lares M., Luparello H. E., Ceccarelli L., Lambas D. G., 2015, MNRAS, 448, 1471

Rykoff E. S. et al., 2014, ApJ, 785, 104

Sahlén M., Zubeldía Í., Silk J., 2016, ApJ, 820, L7

Sánchez C. et al., 2014, MNRAS, 445, 1482

Sheldon E. S. et al., 2004, AJ, 127, 2544

Sheth R. K., van de Weygaert R., 2004, MNRAS, 350, 517

Song H., Lee J., 2009, ApJ, 701, L25

Spolyar D., Sahlén M., Silk J., 2013, Phys. Rev. Lett., 111, 241103

Springel V., 2005, MNRAS, 364, 1105

Sutter P. M., Lavaux G., Wandelt B. D., Weinberg D. H., 2012, ApJ, 761, 44

Sutter P. M., Lavaux G., Hamaus N., Wandelt B. D., Weinberg D. H., Warren M. S., 2014a, MNRAS, 442, 462

Sutter P. M., Pisani A., Wandelt B. D., Weinberg D. H., 2014b, MNRAS, 443, 2983

Tyson J. A., Wittman D. M., Hennawi J. F., Spergelb D. N., 2003, Nucl. Phys. B, 124, 21

Wechsler R. H., 2004, in Mulchaey J. S., Dressler A., Oemler A., eds, Clust. Galaxies Probes Cosmol. Struct. Galaxy Evol. from Carnegie Obs. Centen. Symp. Carnegie Obs. Astrophys. Ser., Pasadena Carnegie Ob

Yang L. F., Neyrinck M. C., Aragón-Calvo M. A., Falck B., Silk J., 2015, MNRAS, 451, 3606

York D. G. et al., 2000, AJ, 120, 1579

Zhao C., Tao C., Liang Y., Kitaura F.-S., Chuang C.-H., 2016, MNRAS, 459, 2670

Zivick P., Sutter P. M., Wandelt B. D., Li B., Lam T. Y., 2015, MNRAS, 451, 4215
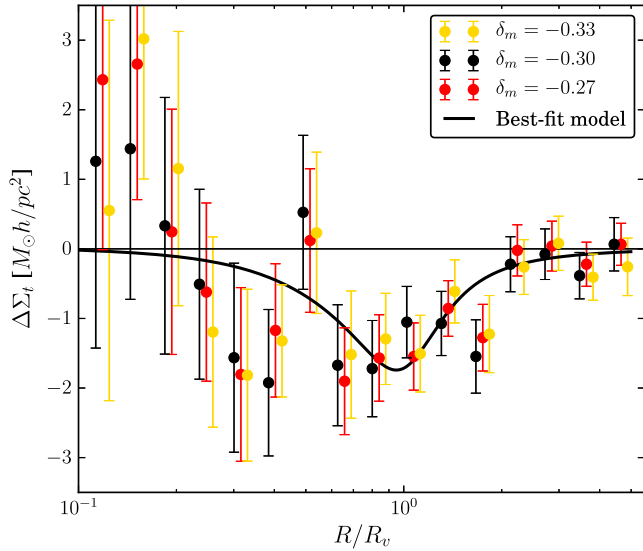
Figure A1. Stacked void lensing signal in DES-SV data for three choices of δ_m: -0.33, -0.30 (fiducial), -0.27. The black line shows the best-fitting model to the fiducial measurement. The comparison shows good agreement between the three sets of measurements.

APPENDIX A: CHOICE OF δ_m

The void finder presented in Section 3 of this paper produces a void catalogue which depends on the chosen value for the maximum density contrast (δ_m) of a pixel to become a void centre (see Section 3.1). The most significant, and hence the deepest voids found by the algorithm are independent of the choice of δ_m, but the total number of voids in the catalogue will vary with that choice. With the fiducial value being $\delta_m = -0.30$, in this appendix, we vary that value by 10 per cent high and low, and test the impact of these changes in the void lensing signal in the data.

The fiducial void catalogue with $\delta_m = -0.30$ contains 78 voids and the goodness of the best-fitting model to its lensing signal (see Section 5.5) is 13.2/14. The catalogue with $\delta_m = -0.33$ contains 73 voids and the goodness of the lensing fiducial best-fitting model is 12.9/14. The catalogue with $\delta_m = -0.27$ contains 107 voids and the goodness of the lensing fiducial best-fitting model is 11.9/14. The good agreement between the lensing signal in the three cases is also shown in Fig. A1.

APPENDIX B: LENSING ON INDIVIDUAL SLICINGS

In Section 4.2, we presented a way of combining different slicings of the LOS, oversampling it with slices of 100 Mpc h^{-1} thickness every 20 Mpc h^{-1}, in order to get more information in that direction. Voids found in neighbouring slices are joined if their centres are close enough, and the resulting group of voids is considered an individual physical underdensity.

In this appendix, we test the impact of that procedure on the void lensing results presented in this paper (Section 5). For that purpose, we perform the lensing measurement on the set of voids found in each individual slicing, corresponding to the five columns
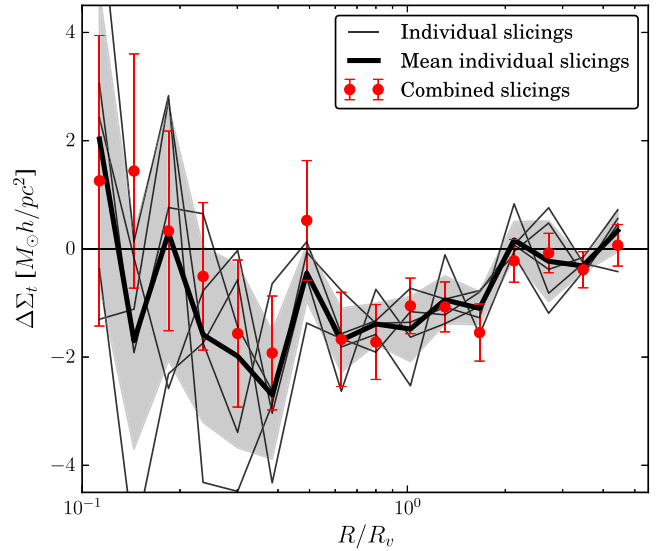

Figure B1. Stacked void lensing signal in DES-SV data for each of the five individual slicings (thin black lines) and for their mean (thick black line), compared to the standard deviation of the individual slicings measurements (shaded grey region). The actual measurement of the final void catalogue from Section 5 is also shown (red data points with errors). This comparison shows good agreement between the combined and individual slicings.

in the graphical representation of Fig. 6. Note that in the case of individual slicings there is no overlap between the slices in which voids are found. The corresponding five lensing measurements, together with its mean and standard deviation, are shown in Fig. B1, where they are compared to the lensing measurement presented in Section 5. The comparison in that plot, with the majority of points from the combined slicings measurement being within 1σ of the mean individual slicings case, shows how the combined slicing approach is not affecting the lensing results in this work in any other way than reducing the noise in the measurement.

APPENDIX C: RANDOMIZED VOID CATALOGUE

The *randomized* void catalogue in this paper is produced such that it mimics the properties of the true void catalogue in redshift and radius. We start from a set of random points inside the data mask; they will constitute the centres of the *randomized* voids. We assign a redshift to each random point drawn for the true redshift distribution of voids and, to each *randomized* void, we assign an angular radius from the true distribution of angular radii for voids of similar redshift (in a window of $\Delta z = 0.1$), this way preserving the redshift–angular radius relation. Finally, from the angular radius and the redshift, we compute the comoving radius of the *randomized* voids.

After this process, we have a *randomized* void catalogue with the same properties as the true one. Then, we also apply the process described in Section 4.1 to get rid of voids near the survey edges. At the end, the *randomized* void catalogue has 10 times as many objects as the true one. Fig. C1 shows the agreement between the distributions of the true and *randomized* voids in redshift and comoving and angular radius.
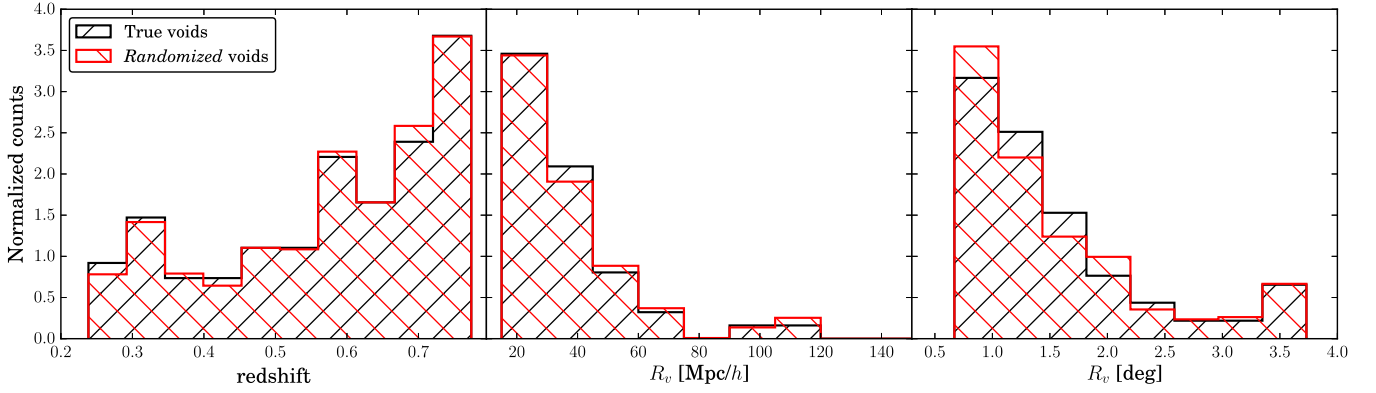
Figure C1. Comparison of the true and randomized void redshift (left-hand panel), comoving radius (centre panel) and angular radius distributions (right-hand panel). The randomized void catalogue is produced to mimic these properties of the true void catalogue by following the procedure explained in Appendix C.

[1]*Institut de Física d'Altes Energies (IFAE), The Barcelona Institute of Science and Technology, Campus UAB, E-08193 Bellaterra (Barcelona), Spain*

[2]*Department of Physics and Astronomy, University of Pennsylvania, Philadelphia, PA 19104, USA*

[3]*Centro de Investigaciones Energéticas, Medioambientales y Tecnológicas (CIEMAT), E-28040 Madrid, Spain*

[4]*Institute of Cosmology and Gravitation, University of Portsmouth, Portsmouth PO1 3FX, UK*

[5]*Kavli Institute for Particle Astrophysics and Cosmology, P. O. Box 2450, Stanford University, Stanford, CA 94305, USA*

[6]*SLAC National Accelerator Laboratory, Menlo Park, CA 94025, USA*

[7]*Universitäts-Sternwarte, Fakultät für Physik, Ludwig-Maximilians Universität München, Scheinerstr. 1, D-81679 München, Germany*

[8]*Department of Physics, University of Michigan, Ann Arbor, MI 48109, USA*

[9]*Department of Physics, ETH Zurich, Wolfgang-Pauli-Strasse 16, CH-8093 Zurich, Switzerland*

[10]*Department of Physics, Stanford University, 382 Via Pueblo Mall, Stanford, CA 94305, USA*

[11]*Department of Physics and Astronomy, University College London, Gower Street, London WC1E 6BT, UK*

[12]*Institució Catalana de Recerca i Estudis Avançats, E-08010 Barcelona, Spain*

[13]*Department of Physics, University of Arizona, Tucson, AZ 85721, USA*

[14]*Brookhaven National Laboratory, Bldg 510, Upton, NY 11973, USA*

[15]*Jodrell Bank Center for Astrophysics, School of Physics and Astronomy, University of Manchester, Oxford Road, Manchester M13 9PL, UK*

[16]*Cerro Tololo Inter-American Observatory, National Optical Astronomy Observatory, Casilla 603, La Serena, Chile*

[17]*Department of Physics and Electronics, Rhodes University, PO Box 94, Grahamstown, 6140, South Africa*

[18]*Fermi National Accelerator Laboratory, P. O. Box 500, Batavia, IL 60510, USA*

[19]*CNRS, UMR 7095, Institut d'Astrophysique de Paris, F-75014 Paris, France*

[20]*Sorbonne Universités, UPMC Univ Paris 06, UMR 7095, Institut d'Astrophysique de Paris, F-75014 Paris, France*

[21]*Carnegie Observatories, 813 Santa Barbara St, Pasadena, CA 91101, USA*

[22]*Laboratório Interinstitucional de e-Astronomia – LIneA, Rua Gal. José Cristino 77, Rio de Janeiro RJ - 20921-400, Brazil*

[23]*Observatório Nacional, Rua Gal. José Cristino 77, Rio de Janeiro RJ - 20921-400, Brazil*

[24]*Department of Astronomy, University of Illinois, 1002 W. Green Street, Urbana, IL 61801, USA*

[25]*National Center for Supercomputing Applications, 1205 West Clark St, Urbana, IL 61801, USA*

[26]*Institut de Ciències de l'Espai, IEEC-CSIC, Campus UAB, Carrer de Can Magrans, s/n, E-08193 Bellaterra, Barcelona, Spain*

[27]*School of Physics and Astronomy, University of Southampton, Southampton SO17 1BJ, UK*

[28]*Excellence Cluster Universe, Boltzmannstr. 2, D-85748 Garching, Germany*

[29]*Faculty of Physics, Ludwig-Maximilians-Universität, Scheinerstr. 1, D-81679 Munich, Germany*

[30]*Department of Astronomy, University of Michigan, Ann Arbor, MI 48109, USA*

[31]*Kavli Institute for Cosmological Physics, University of Chicago, Chicago, IL 60637, USA*

[32]*Center for Cosmology and Astro-Particle Physics, The Ohio State University, Columbus, OH 43210, USA*

[33]*Department of Physics, The Ohio State University, Columbus, OH 43210, USA*

[34]*Australian Astronomical Observatory, North Ryde, NSW 2113, Australia*

[35]*Departamento de Física Matemática, Instituto de Física, Universidade de São Paulo, CP 66318, CEP 05314-970, São Paulo, SP, Brazil*

[36]*George P. and Cynthia Woods Mitchell Institute for Fundamental Physics and Astronomy, and Department of Physics and Astronomy, Texas A&M University, College Station, TX 77843, USA*

[37]*Department of Astrophysical Sciences, Princeton University, Peyton Hall, Princeton, NJ 08544, USA*

[38]*Jet Propulsion Laboratory, California Institute of Technology, 4800 Oak Grove Dr., Pasadena, CA 91109, USA*

[39]*Department of Physics and Astronomy, Pevensey Building, University of Sussex, Brighton BN1 9QH, UK*

[40]*ICTP South American Institute for Fundamental Research Instituto de Física Teórica, Universidade Estadual Paulista, 01140-070 São Paulo, Brazil*

[41]*Computer Science and Mathematics Division, Oak Ridge National Laboratory, Oak Ridge, TN 37831, USA*

[42]*Max Planck Institute for Extraterrestrial Physics, Giessenbachstrasse, D-85748 Garching, Germany*

This paper has been typeset from a TeX/LaTeX file prepared by the author.